

See discussions, stats, and author profiles for this publication at: <https://www.researchgate.net/publication/277364994>

Composite Catalyst Surfaces: Effect of Inert and Active Heterogeneities on Pattern Formation

ARTICLE *in* THE JOURNAL OF PHYSICAL CHEMISTRY · DECEMBER 1996

Impact Factor: 2.78 · DOI: 10.1021/jp961689q

CITATIONS

54

READS

6

6 AUTHORS, INCLUDING:



Markus Bär

Physikalisch-Technische Bundesanstalt

180 PUBLICATIONS 3,724 CITATIONS

SEE PROFILE



Harm Hinrich Rotermund

Dalhousie University

140 PUBLICATIONS 5,071 CITATIONS

SEE PROFILE

Composite Catalyst Surfaces: Effect of Inert and Active Heterogeneities on Pattern Formation

M. Bär

Max-Planck-Institut für Physik komplexer Systeme, Bayreuther Strasse 40, Haus 16, 01187 Dresden, Germany

A. K. Bangia and I. G. Kevrekidis*

Department of Chemical Engineering, Princeton University, Princeton, New Jersey 08544-5263

G. Haas, H.-H. Rotermund, and G. Ertl

Fritz-Haber-Institut der Max-Planck-Gesellschaft, Faradayweg 4-6, 14195 Berlin, Germany

Received: June 10, 1996; In Final Form: September 18, 1996[®]

Spatiotemporal dynamics in reaction–diffusion systems can be altered through the properties (reactivity, diffusivity) of the medium in which they occur. We construct active heterogeneous media (composite catalytic surfaces with inert as well as active inclusions) using microelectronics fabrication techniques and study the spatiotemporal dynamics of heterogeneous catalytic reactions on these catalysts. In parallel, we perform simulations as well as numerical stability and bifurcation analysis of these patterns using mechanistic models. At the limit of large heterogeneity “grain size” (compared to the wavelength of spontaneously arising structures) the interaction of patterns with inert or active boundaries dominates (e.g., pinning, transmission, and boundary breakup of spirals, interaction of pulses with corners, “pacemaker” effects). At the opposite limit of very small or very finely distributed heterogeneity, effective behavior is observed (slight modulation of pulses, nearly uniform oscillations, effective spirals). Some representative studies of transitions between the two limits are presented.

I. Introduction

The study of spontaneous generation of spatiotemporal patterns in open, nonequilibrium systems is an established field of research in many areas of physics (convection in liquids, liquid crystals, and binary mixtures), chemistry (reactions in solutions, in gels, and on catalytic surfaces), and biology (morphogenesis, aggregation of amoebas and bacteria, excitation waves in neuronal and cardiac tissue).^{1,2} While traditionally instabilities leading to pattern formation have been studied in media with spatially uniform and temporally constant properties (*i.e.*, through partial differential equations with constant coefficients), current research increasingly explores how spatiotemporal dynamics are influenced through externally imposed spatial gradients (e.g. ref 4), temporal forcing (e.g. ref 5), or feedback schemes (e.g. ref 6). In our recent experimental and numerical studies, we have explored the use of microstructured and composite surfaces to effectively alter pattern dynamics during the oxidation of CO on single crystal Pt(110) surfaces.^{7,8} The underlying premise is that active reaction–diffusion media can be constructed containing inert (no-flux) passive (diffusion only), or active inclusions and that the scale, geometry, and nature of these heterogeneities can drastically affect spontaneous pattern formation on the new composite medium.

The behavior of chemical concentration fronts in heterogeneous reactive media has been investigated for a variety of geometries in theoretical⁹ as well as experimental¹⁰ and computational studies;¹¹ in excitable media that support spirals and pulses, the influence of small scale heterogeneities on the dynamics of rotating spirals has also been studied.¹² In Rayleigh–Bénard convection, experiments^{13,14} as well as theoretical analysis¹⁵ have revealed that modulations of the aspect

ratio on a scale comparable to the roll wavelength can lead to changes of the pattern dynamics (drifting rolls and resonance phenomena). Similar dynamical phenomena have also been reported in studies of striped semiconductor lasers.¹⁶

CO oxidation on the Pt(110) surface as well as a variety of other catalytic reactions on single crystal surfaces has been known to exhibit spontaneous pattern formation for a wide range of operating conditions.^{17–19} For instance, the spatiotemporal structures found during CO oxidation on Pt(110) range from fronts, pulses, spirals, and standing waves to chemical turbulence^{20,21} in accordance with standard reaction–diffusion phenomenology.^{1–3} In this work we present and discuss selected examples of CO oxidation in complicated microstructured geometries as well as in heterogeneous (composite) catalytic surfaces. The composite surfaces are formed by combining different components whose individual catalytic activities are coupled through surface diffusion. The paper is organized as follows: section 2 is a brief discussion of the experimental procedure and the catalyst fabrication; section 3 presents a simplified mechanistic model and the types of solutions it predicts, defines the relevant spatial scales, and sets the stage for the type of bifurcation/instability analysis that follows. In section 4 we study the behavior of spirals in media containing periodic grids of inert inclusions. In section 5 the influence of sharp corners on the no-flux boundaries on the propagation of planar waves is discussed. Results on the behavior of chemical waves in composite media are then presented in section 6, and the paper concludes with a brief discussion.

II. Experiment

The experiments were performed on Pt(110) single crystal surfaces, on which microstructured reacting domains were

[®] Abstract published in *Advance ACS Abstracts*, November 1, 1996.

constructed as follows: after depositing an 80–100 nm thick titanium layer on the Pt surface, a negative photoresist process was used to uncover regions of bare Pt. Standard cleaning procedures were then applied to the sample in an ultrahigh-vacuum chamber. The reaction temperature and the partial pressures of carbon monoxide and oxygen were kept constant throughout the experiment. Microcomposite surfaces have been constructed in two distinct ways: (a) by deposition of submonolayer coverages of Au on parts of the Pt crystal and (b) by sputtering a nanometer-thick Ti layer partially covering the surface down to monolayer or submonolayer coverages. The spatiotemporal dynamic behavior was observed through photoemission electron microscopy (PEEM),²² a technique that combines high temporal (25 ms, limited by the video frequency) with submicron spatial resolution (0.2 μm) and a field of view up to $800 \times 800 \mu\text{m}^2$. In the PEEM images, oxygen-rich regions appear dark and CO-rich areas appear light gray as a result of local differences in the work function (the energy required to remove an electron from the metal surface) caused by the different adsorbates and adsorbate coverages.

III. The Model

Taking into account Langmuir–Hinshelwood elementary adsorption, desorption, and reaction steps,²³ as well as the change in surface structure (surface reconstruction lifting as a result of CO adsorption) and surface diffusion in two dimensions, a mechanistic model of the catalytic CO oxidation on Pt surfaces has been proposed.^{24,25} A simplification of this model, describing the dynamics of adsorbate coverage on the surface, u , and surface structure (fraction w of 1×1 surface, lifting the reconstruction from 1×2 clean Pt(110)) is given by

$$\frac{\partial u}{\partial t} = \frac{1}{\epsilon} u(1-u) \left(u - \frac{w + b(x,y)}{a} \right) + \nabla(D \cdot \nabla u) \quad (1)$$

$$\frac{\partial w}{\partial t} = f(u) - w \quad (2)$$

with $f(u)$ for typical excitable conditions defined by

$$f(u) = \begin{cases} 0 & \text{if } u < 1/3 \\ 1 - 6.75u(u-1)^2 & \text{if } 1/3 \leq u \leq 1 \\ 1 & \text{if } u > 1 \end{cases} \quad (3)$$

All variables in this simplified model have been made dimensionless using appropriate scales for the physical variables; typically $u = 0$ corresponds to a CO(O) surface coverage of 0.65 (0.02) monolayers (ML), whereas $u = 1$ represents a 0.2 ML (0.25 ML) of CO(O) coverage for the set of parameters used here. The dimensionless time and space units correspond approximately to 2 s and 1 μm , respectively. The operating conditions—CO partial pressure p_{CO} , oxygen partial pressure p_{O_2} , and surface temperature T —are embedded in the dimensionless parameters a , b , and ϵ in the above equations. a controls whether the system is possibly bistable ($a > 1$) or oscillatory and excitable ($a < 1$). While all parameters affect the stability of the steady state solutions, b specifically describes the balance of the CO and oxygen on the surface; ϵ represents a ratio of evolution time scales for the system variables u and w . $b = 0$ corresponds to equal amounts of both adsorbates, while $b > 0$ ($b < 0$) indicates dominance of CO(O) on the surface. The inert domain boundaries are modeled by no-flux boundary conditions. Composite surfaces are modeled through spatially varying kinetic parameters, while the diffusion constants are considered identical for the two components of a composite

medium; observations of spiral waves crossing grain boundaries in our experiments appear to corroborate this assumption. Numerical simulations in one spatial dimension have been performed using pseudospectral discretization of the governing equations and the method of lines with implicit integrators (like ODESSA²⁷) for the time evolution. Typically, the distance between collocation points has been chosen to be ≈ 0.31 , i.e., 128 collocation points over a length $L = 40.0$. Finite difference spatial discretization with simpler explicit integrators have been used for studies in two dimensions; there a spatial discretization $\Delta x \approx 0.2$ and a time step of 4×10^{-3} have been used. Convergence of the results with respect to finer discretization has been tested for both cases. The gray scale code used for simulation results displays CO (O) rich as white (black), in analogy with the experimental images.

The subject of this work is a study of the interaction of the substrate length scales, imposed through patterning of the reactive surface, with the length scales of spontaneously excited spatiotemporal reaction–diffusion patterns. In what follows we will refer to the former as the “substrate length scales” and the latter as the “dynamic length scales”. For periodic composites in one and two dimensions the substrate length scales (l_h) are the ones associated with the composite geometry: the characteristic dimensions of a unit cell; for anisotropic composites $l_h^x \neq l_h^y$. Dynamic length scales depend on the type of pattern under consideration (alternatively, on the region of a – b – ϵ parameter space of eqs 1–3). The “excitable medium” paradigm is formulated at the small ϵ limit, where the interface width of a front separating a high- u from a low- u state is of the order of the dimensionless “diffusion length” $l_D = 4\sqrt{2D\epsilon}$. This quantity is derived assuming a constant inhibitor concentration near the activator front and solving the resulting scalar partial differential equation with a cubic reaction term.^{3,26} In the general case of anisotropic diffusion, an l_D^i has to be defined for each principal axis denoted by the superscript i . In the above formula D is then replaced by D_{ii} , the i th diagonal element of the diffusion tensor D . For the parameters used here ($a = 0.84$, b small, $\epsilon = 0.025$, and $D = 1$), this characteristic length is of order one ($l_D = 0.9$). Other representative “dynamic length scales” are the width of a solitary pulse in one dimension and the wavelength λ of stable spirals in a homogeneous two-dimensional medium. Both values range between 5 and 10 space units for the examples discussed here. The ratios of the substrate length scales to the dynamic length scales can thus be defined. In the limit $\delta \rightarrow \infty$ the homogeneous medium is recovered; however, novel effects at the boundary may emerge. In the opposite limit $\delta \rightarrow 0$, we expect the composite medium to exhibit homogenized behavior. For $\delta \sim 1$, where the two length scales interact strongly, one might expect nontrivial spatiotemporal dynamics. The essential bifurcation parameter in the following sections is $\delta_\lambda = l_h/\lambda$, while for the composite media discussed in the last section $\delta_D = l_h/l_D$ will play this role.

IV. Spiral Waves in a Medium with a Periodic Array of Inert Inclusions

The first “complex geometry” for which experiments were performed on microstructured surfaces was a fixed grid of inert, $\sim 7 \mu\text{m}$ Ti squares with a lattice constant (distance between the centers of neighboring sites) of $20 \mu\text{m}$; some observations of spiral waves in such a grid have been previously reported in ref 7 and 8. In the phenomena described here the substrate length scale is constant, and the dynamic length scale (spiral wavelength) is changed through variation of the operating conditions. As this scale changes, states with coexisting free

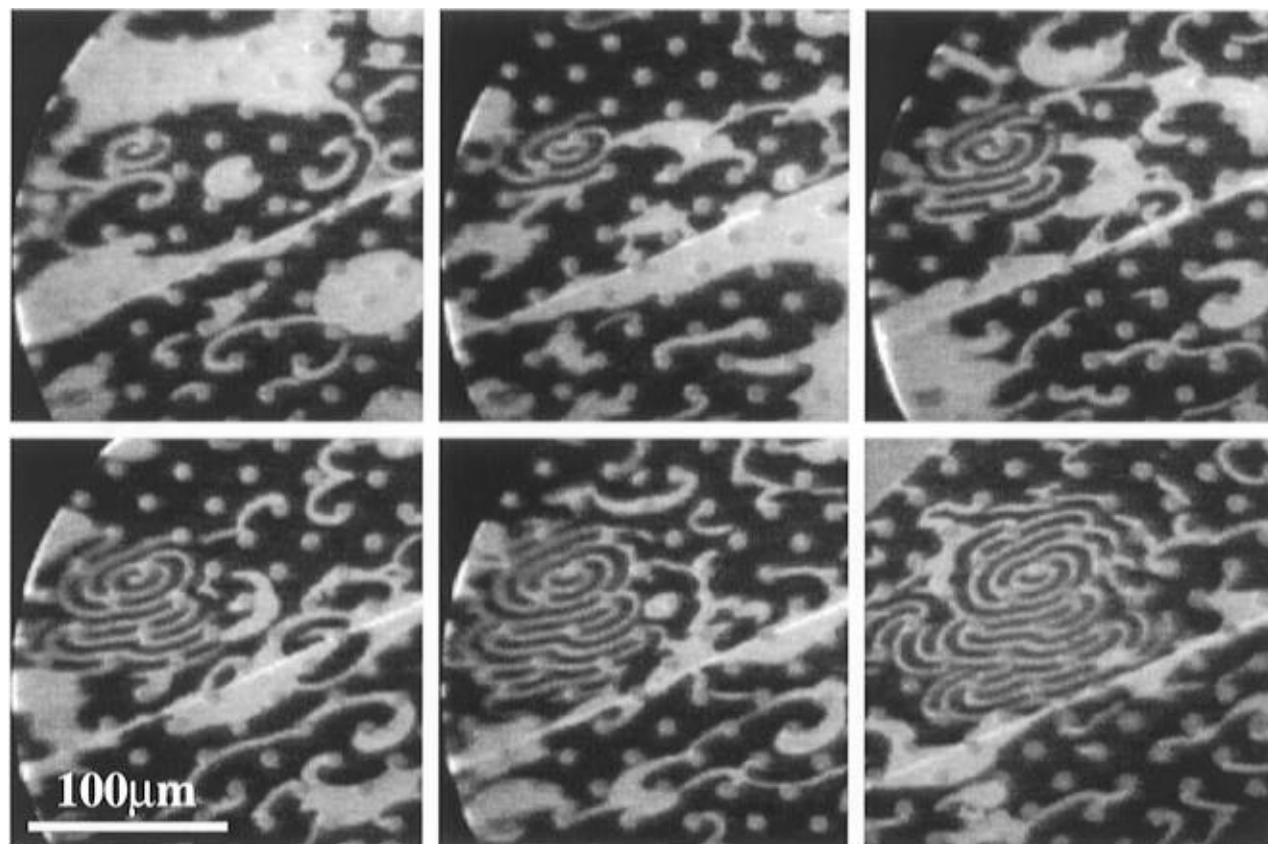


Figure 1. PEEM images showing evolution of a free spiral on Pt(110) surface and its interaction with an inert grid of Ti inclusions. The lattice constant (distance between the centers of two neighboring inclusions) is $20\ \mu\text{m}$, and the grid element diameter is $\sim 7\ \mu\text{m}$. Experimental conditions are $T = 425\ \text{K}$, $p_{\text{CO}} = 2.4 \times 10^{-5}\ \text{mbar}$, and $p_{\text{O}_2} = 4.0 \times 10^{-4}\ \text{mbar}$. The frames are 20 s apart.

spirals and spirals pinned to the inclusions as well as states with only pinned spirals are observed on the surface; the pinned spirals in experiments are frequently multiarmed.

In parallel with experimental observations, we present a numerical investigation of the fate of an ensemble of free spirals when a grid of periodic inert (no flux) inclusions of varying size and density is imposed. This yields statistics of the number of eventually persisting free spirals. These calculations will show that a form of transition from states with free spirals to ones with only pinned spirals develops depending on the parameters of the geometry (lattice constant, inclusion size). The experiments have been conducted by gradually increasing the partial pressure of CO at fixed temperature and oxygen partial pressure. First, fronts of predominant CO coverage start to propagate but are annihilated by the coexisting (faster) oxygen fronts. Only when the CO pressure is large enough to yield CO fronts at speeds comparable to that of the oxygen fronts may spirals form. (Details of the transition from fronts to spirals in homogeneous media were described in earlier publications.^{21,28}) Figure 1 shows an example of the temporal evolution of the interaction of a free spiral with the inert grid. The free spiral acts as a source of periodic waves on the grid surface; these waves interact strongly with the grid elements, and after sufficient time elapses (much longer than the sequence in Figure 1) the final state exhibits several pinned four-armed spirals. Figures 2a,b displays experiments in a different parameter regime where pinned spirals dominate the surface. In the lower panels of Figure 2, a transient starting (c) from a state dominated by one-armed free spirals is eventually taken over (d) by pinned two-armed spirals. The observation of multiarmed, pinned spirals might, at first glance, seem surprising since we have not observed spontaneous formation of multiarmed spirals in simulations of a homogeneous medium with zero flux inclusions.

It would be interesting to study the effect of slight asymmetries/inhomogeneities in the medium on the formation and persistence of these multiarmed spirals. The interaction of wave trains originating from different sources (free and/or pinned spirals) traveling across (and modulated by) the inert grid also gives rise to intricate spatiotemporal dynamics. (For studies of the interaction of competing waves see, for example, refs 25 and 29–31.)

In the second part of this section, we present numerical simulations of the evolution of a large spiral population within a grid of inert inclusions. We choose parameters typical for excitable conditions given by $a = 0.84$, $b = 0.07$, and $\epsilon = 0.025$. In the simulations we choose to vary the ratio of length scales by keeping the active medium properties (dynamic scales) constant and vary the substrate length scale (the density of inclusions as well as their size) systematically. In addition, a 1:4 anisotropy in the diffusion constant is chosen ($D_x = D_{11} = 1$ and $D_y = D_{22} = 0.25$), and an angle of 45° between the lattice axes and principal diffusion (crystal symmetry) axes is imposed, consistent with the experimental observations for Pt(110) above.

The initial condition, a state with ~ 85 randomly distributed free spirals, is characteristic of the spatiotemporal dynamics of the active medium at these parameter values and was obtained after transient integration in such a homogeneous medium. These spirals interact only weakly, and their number density remains approximately constant in the homogeneous medium. In heterogeneous media, however, a certain percentage of the spirals get trapped by the presence of inclusions. After a longer transient (typically of the order of 10–20 periods of rotation of a free spiral in the medium) a stationary pattern emerges, characterized (depending on conditions) either by many free spirals or by essentially all waves pinned to the inert inclusions. The remaining free spirals are counted, and their (approximately

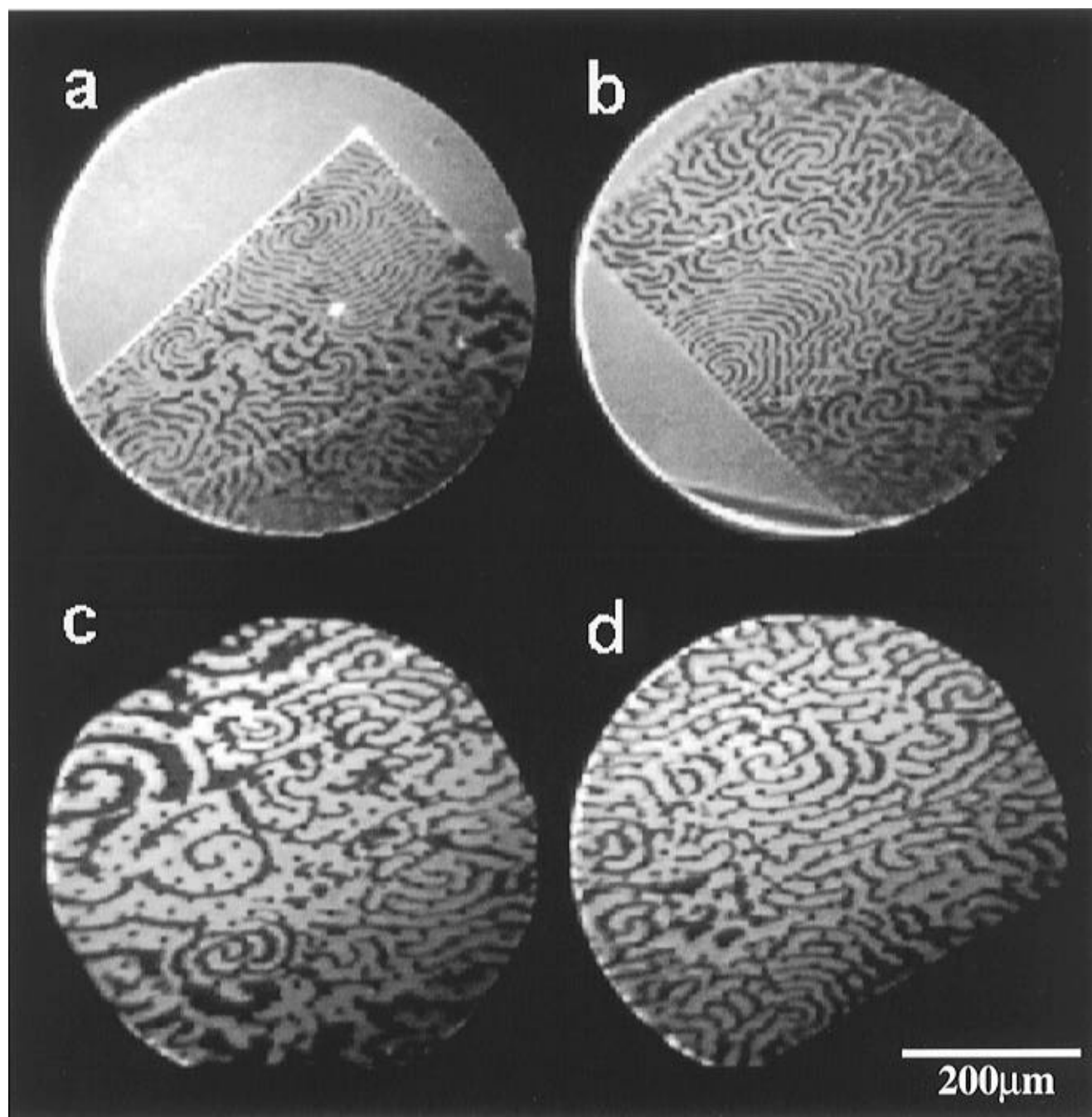


Figure 2. (a, b) Snapshots of different parts of the surface showing evolution of waves on Pt(110) with an inert grid of Ti squares. (The boundaries of the area containing the grid are clearly visible.) Experimental conditions are the same as in Figure 1 except $p_{\text{CO}} = 2.7 \times 10^{-5}$ mbar. (c, d) Transient snapshots approximately 3 min apart for a different set of operating conditions: $T = 451$ K, $p_{\text{CO}} = 3.32 \times 10^{-5}$ mbar, and $p_{\text{O}_2} = 4 \times 10^{-4}$ mbar; the correlation between the pattern wavelength and the lattice constant clearly becomes stronger as time evolves.

stationary) number is plotted against the number of inclusions on a fixed total area of the array for different sizes of the inclusions (Figure 3). All the data are well represented by a linear relationship that links the number of surviving free spirals n_{sp} to the number of inert inclusions n_{sq} with

$$n_{\text{sp}} = n_0(1 - n_{\text{sq}}(d + f)^2/A)$$

where n_0 is the number of spirals in the initial condition, d is the side length of a square inclusions, and A is the total area of the array. f is an independent fit factor which can be rationalized as a "spiral trapping length": $f/2$ is the minimum distance of a free spiral core from a grid element for the spiral to escape trapping and remain visible as a free spiral. Cast in these terms, the density of spirals remains constant if an "effective area",

the original one reduced by $n_{\text{sq}}(d + f)^2$, is considered. The quantity f obtained from the linear fits in Figure 3 turned out to be almost independent of the size of the squares used. Its value varies between 3.3 and 3.8 space units (4–5 μm) for the parameters used in the simulations. At the same time, the wavelength of a free spiral in the homogeneous medium ranges between approximately 8 and 4 space units (10 and 5 μm , respectively) when both the fast and the slow diffusion directions are considered. Obviously, the lattice constant should be larger than $(d + f)$ to allow for existence of free spirals based on this simple argument; the results derived from Figure 3 indicate that the distance between two inclusions should be somewhat larger than the free spiral wavelength λ . For comparison, in the experiment shown in Figure 1 this distance is 13 μm while the free spiral wavelength along the grid axes is roughly 10 μm .

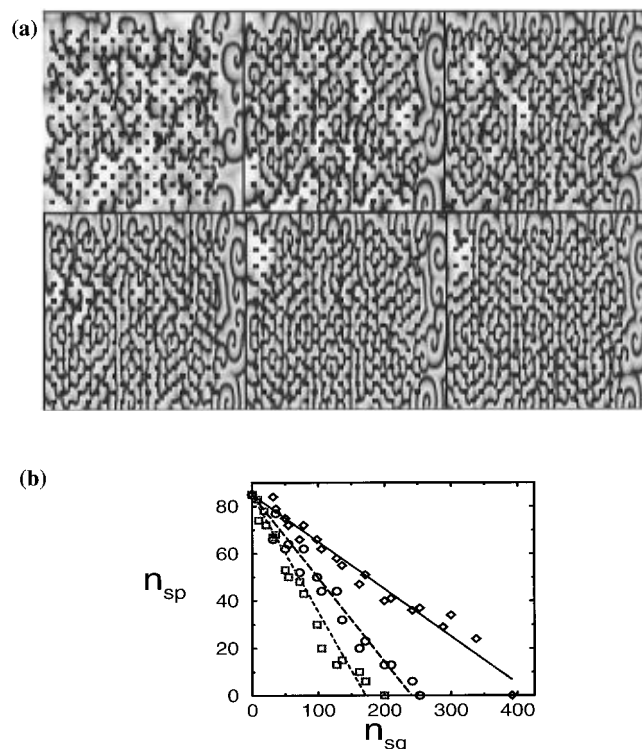


Figure 3. Numerical simulations with $a = 0.84$, $\epsilon = 0.025$, and $b = 0.07$ for a square catalyst surface with dimensionless side length $L = 100$. The top panels display a sequence of snapshots from the transient evolution of an initial condition with ~ 85 free spirals when a grid of inert square inclusions is imposed. The time difference between frames is roughly 1 spiral period (6 time units). The bottom figure shows a fit of the statistics of the approximate number n_{sp} of ultimately surviving free spirals as a function of the number n_{sq} of inclusions in the grid as described in the text. A good fit of the data can be obtained for square grid elements with dimensionless side length 1.17 (square symbols), 2.73 (open circles), and 4.29 (open rhombi) with a single fitting parameter, the “trapping length” f (see text).

The above considerations should only hold for a finite range of inclusion sizes; if the inclusions are too small (*e.g.*, much smaller than the core diameter of the free spiral), they should not be able to pin spirals and would therefore have a much lesser effect on the overall behavior. If, on the other hand, the square side becomes comparable to the lattice constant, the little remaining “free area” cannot support free spirals.

Motivated by the experimental observations in Figure 1, we investigated numerically the behavior of spirals pinned to square-shaped no-flux inclusions. A free spiral from a uniform medium simulation was pinned on an imposed square no-flux inclusion. As the perimeter (the dimensionless side length) of the inclusion was varied, the overall rotation period of the pinned spiral varied almost linearly with it. In dimensional units, for a pinning square of side length $1.47 \mu\text{m}$ ($11.25 \mu\text{m}$) it was 10.6 s (43.6 s). For an inclusion size of $7.3 \mu\text{m}$ (close to experimental grid element size, $\sim 7 \mu\text{m}$), the computational period was 30.1 s, close to 4 times the period of the free spiral (7.7 s).

V. Microstructures: Wave Trains at Sharp Corners

When the substrate length scale is larger than the dynamic scale, patterns typically “feel” only a part of the grain boundary, and therefore boundary effects play a major role in determining pattern dynamics. For example, abrupt changes in the geometry of the boundaries can induce large curvature on propagating wave trains. This can result in the breakup or reversal of waves or other new forms of behavior of reaction–diffusion waves near obstacles. In a recent publication,³² we studied the behavior

of concentration fronts at the exit of narrow channels into large, two-dimensional domains: the curvature caused by such a transition in geometry can lead to slowdown or even reflection or breakup of the fronts. An alternative way to probe the effects of curvature on wave propagation is to construct “T-junctions” as a model geometry. In Figure 4 the experimental image of a spiral in the upper left arm of a (rotated) H-shaped Pt domain is seen; the boundary is an inert Ti wall. The spiral acts as a source of a periodic wave train that can be seen to travel around several corners in the domain. While the waves at two of the right angles they encounter stay attached to the boundary as they progress, some of the waves turning to the right at the bottom T-junction show an instability and retract from the boundary. A series of snapshots in Figure 4 show the time evolution of waves at this corner. The anisotropy of the diffusion constant is observed to play an important role in the instability: there is a distinct difference in the shape and curvature of the waves on opposite sides of the bottom T-junction, as well as in the angle they form with the respective boundaries. The angle of incidence near the corner appears to correlate with the decollation instability: wave trains that do not detach from the boundary as they round corners appear almost vertical to, and propagate almost parallel to, the boundary. The ones which develop an instability approach the boundary at an apparent angle of $\sim 30^\circ$.

Numerical experiments in a related geometry (displayed in Figure 5) have been performed by imposing a wave source via a Dirichlet boundary condition (fixed values of u and w in the excited state of the medium) at the left end of the domain. A deep “groove” in the bottom channel wall introduces corners for the wave trains to interact with. At higher excitability (lower values of b , Figure 5a), the waves curve strongly at the corner while still remaining attached to the no-flux boundary. At slightly lower excitability (Figure 5b), the abrupt change at the corner results in the detachment of the waves from the boundary. The open end of the wave curls up to form a spiral wave in the groove that coexists with the planar wave train persisting in the upper channel. This phenomenon of spiral creation due to wave train “decollation” at a sharp corner has also been observed in experiments with the Belousov–Zhabotinsky reaction.³⁴ At even weaker excitability, the new “mode” that forms in the groove finally invades the flow of the periodic wave train leading to irregular behavior over the entire domain (Figure 5c).

Principal component analysis (Karhunen–Loève expansion³⁵) of snapshot ensembles from numerical simulation yields “coherent structures” (eigenfunctions of the two-point correlation matrix) which succinctly summarize the different types of behavior (also displayed in Figure 5). The two modes in Figure 5a (one each from the first two pairs of space-shifted modes) confirm the periodic, almost traveling wave nature of the solution, while the pattern in Figure 5b possesses competing localized coherent modes with different frequencies and appears quasiperiodic. Such a sustained coexistence of wave patterns with different temporal frequencies is relatively rare in reaction–diffusion systems; usually, the source with higher frequency suppresses the one with lower frequency (see *e.g.* refs 21 and 25). In this case, however, the spiral mode in the groove survives, interacting only laterally with the open ends of the waves initiated at the left channel boundary. The “corner instability” or “wave decollation” depends strongly on the frequency of the incoming waves: the higher the frequency, the easier it is for the wave edge to detach from the no-flux boundary. A more systematic theoretical investigation should also take into account anisotropy of diffusion and relative

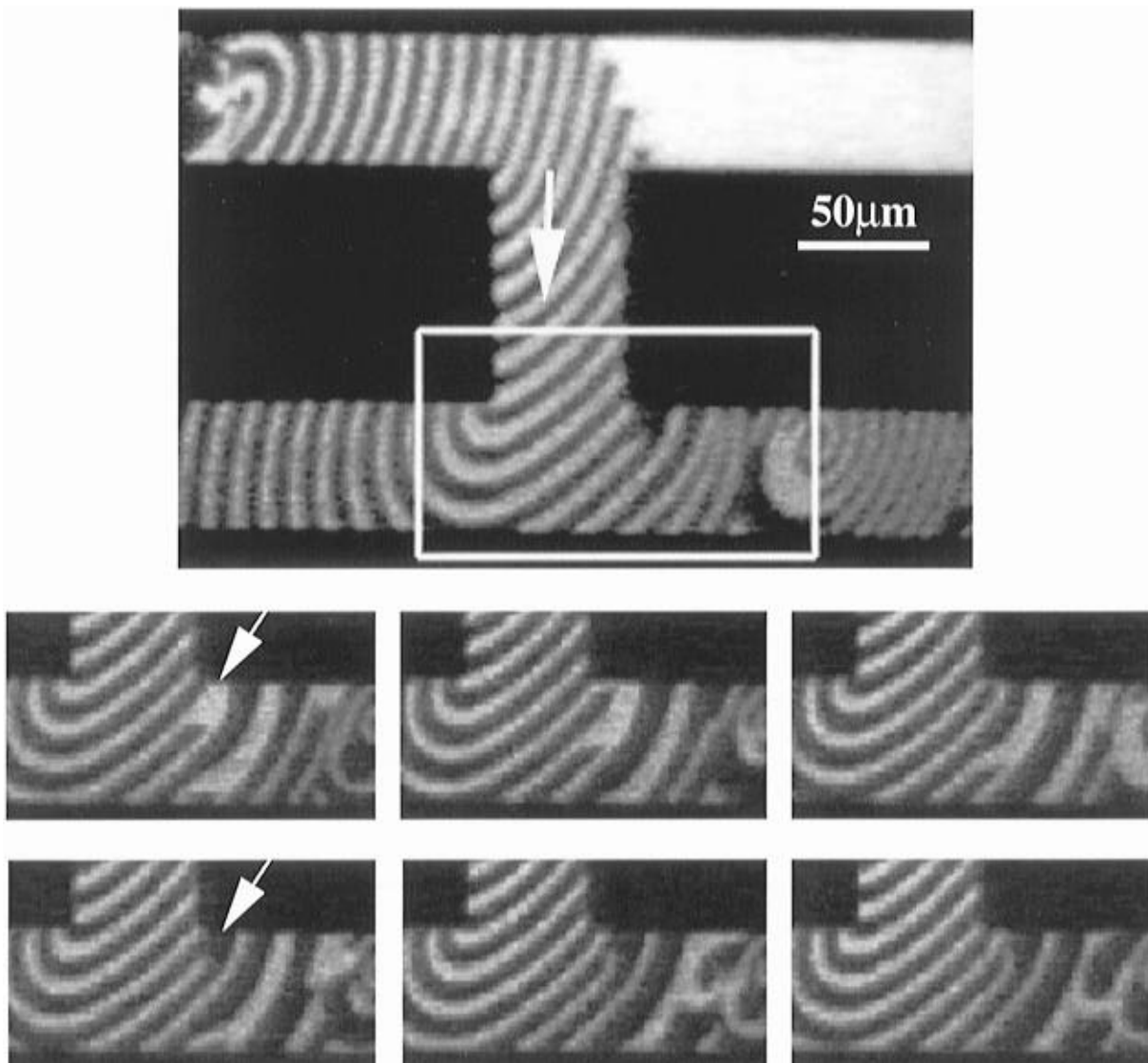


Figure 4. Concentration wave trains “rounding corners” in a (rotated) H-shaped Pt domain surrounded by tall (800 Å) inert Ti walls (black). The sequence of lower panels (magnifications of the area marked in the upper panel) shows an instability: some of the waves detach and retract from the corner boundary. The experimental conditions are $p_{O_2} = 4 \times 10^{-4}$ mbar, $p_{CO} = 5 \times 10^{-5}$ mbar, and $T = 440$ K. The time difference between frames in the lower panel is 4 s.

orientation of the corner with respect to the principal diffusion axes. Analyzing snapshot sequences for the case shown in Figure 5c does not produce a stationary set of modes, indicating presumably “turbulent” (high-dimensional spatiotemporally chaotic) behavior; the number of modes needed to capture the space–time dynamics increases considerably.

Figure 6 shows a qualitatively similar scenario in the case of a wave train in a channel geometry with a narrow slit opening; here perturbation in the boundary is provided by a vertical barrier in the middle of the channel. While at higher excitability the wave train wraps around the barrier staying attached to the boundary (Figure 6a), lower values of excitability result in the detachment of waves at the slit and formation of another mode behind the barrier (Figure 6b,c). The structure and energy content of the two coherent modes (again, one each from the first two space-shifted pairs of modes) are also displayed in Figure 6. The dynamics change from periodic to quasiperiodic and eventually to spatiotemporally apparently chaotic for decreasing values of excitability. It is obvious that the interaction of reaction–diffusion fronts and pulses with inert boundaries can be truly rich and variegated; the propagation speeds of such fronts in random networks of passages can vary drastically in such nontrivial geometries.

VI. Pattern Formation in Composite Media

The experiments and modeling results presented so far have been based on geometries modified with inert inclusions that are modeled through no-flux boundary conditions. A natural next step is to consider inclusions (heterogeneities) which allow adsorbate transport across them via surface diffusion—thus, the dynamics on different reactive regions of the surface are coupled at length scales comparable to the diffusion length. An experimental realization of this type of reactive/passive composite has been recently used for BZ reaction studies.³⁸ If, in addition, the heterogeneous inclusions also happen to be reactive, then surface diffusion couples the catalytic dynamics of different surface components. Composite catalyst surfaces of this type have been constructed by means of submonolayer converges of Au or Ti on Pt(110) for CO oxidation.^{36,37} Experiments so far have dealt with the case of coupling of relatively large domains and investigations of the behavior of a single “grain boundary”. Many of the experimentally observed effects have been reproduced with our simplified reaction–diffusion model.³¹

Here we consider certain case studies of microcomposite surfaces at substrate length scales comparable to instability

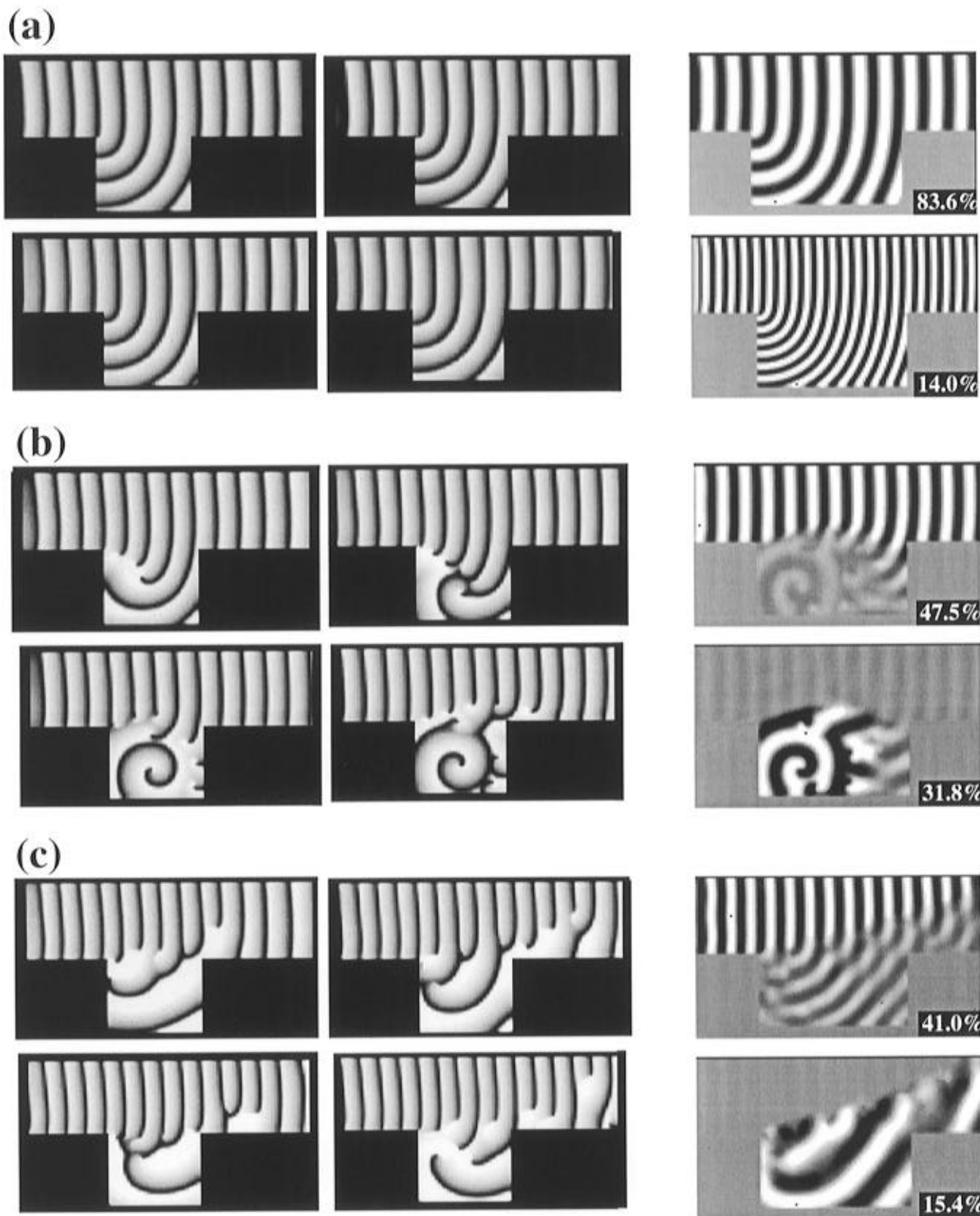


Figure 5. Numerical simulations of a wave train in a grooved channel for (a) $b = 0.16$, (b) $b = 0.18$, and (c) $b = 0.20$; the remaining model parameters for all simulations are fixed at $\epsilon = 0.025$, $a = 0.84$, and $D_x = D_y = 1.0$. The length of the channel is 100 units, its width 25 units, and the depth of the groove 25 units. The time difference between frames is 8.3 time units or about 1 temporal period of the wave source at the left boundary. One mode each of the first two pairs of Karhunen–Loève modes, obtained from a series of 200 snapshots covering a time interval of 96 time steps (12 temporal periods of the wave source at the left boundary) of a grooved channel simulation (and the corresponding “energy content”), are displayed on the right.

wavelengths typical for catalysis on the clean metal surface. In particular, we distribute two catalysts with different surface properties (reactivity, diffusivity) in the form of micrometer-wide stripes or checkerboards and study pattern dynamics on

such a surface and its dependence on the imposed wavelength (the width of the stripes or squares). Such a spatial modulation of surface properties is practically feasible in experiments with composite catalysts. For simplicity in computational studies,

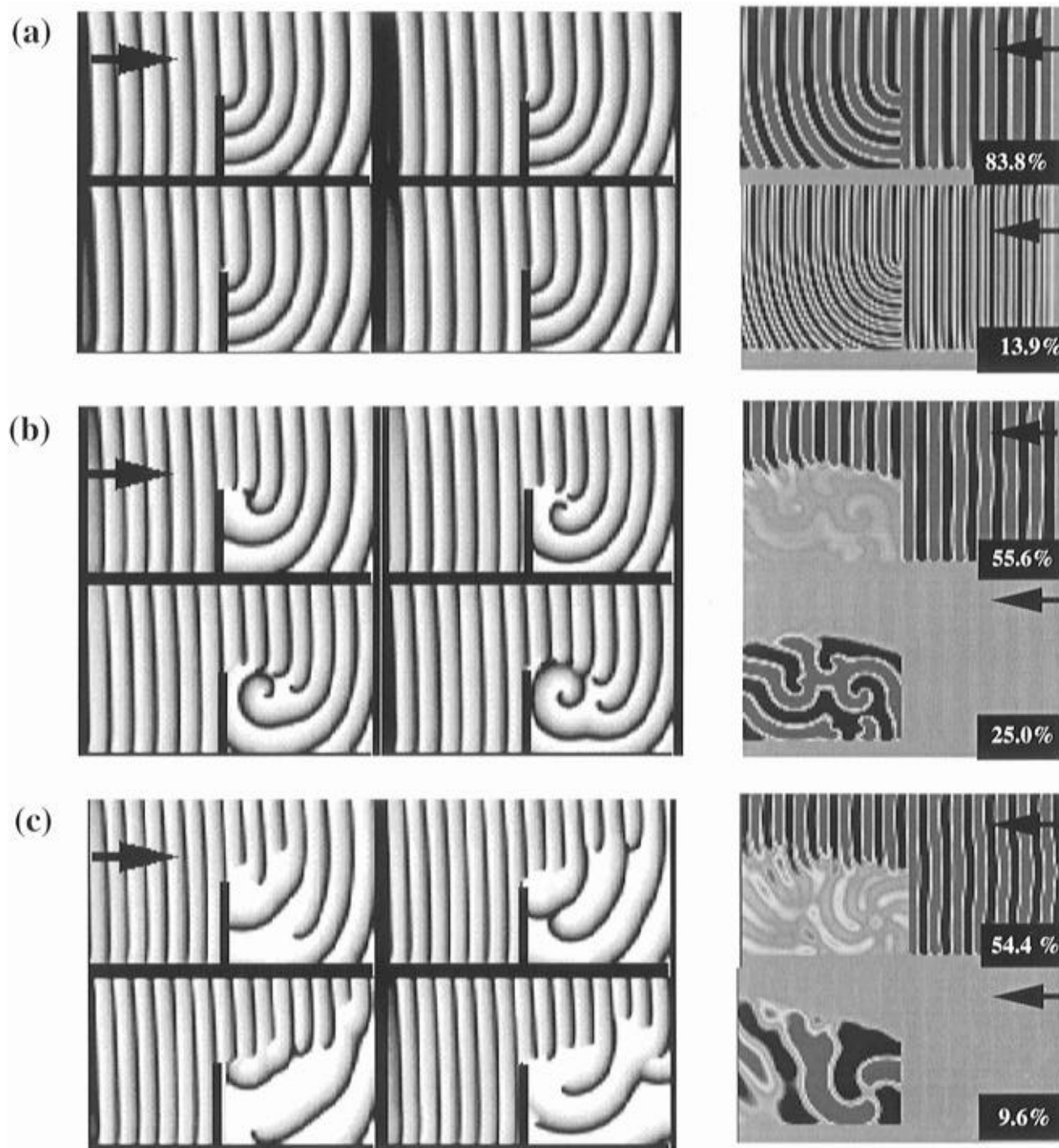


Figure 6. Numerical simulations of a wave train in a slit geometry for (a) $b = 0.16$, (b) $b = 0.18$, and (c) $b = 0.20$; the remaining model parameters for all simulations are fixed at $\epsilon = 0.025$, $a = 0.84$, and $D_x = D_y = 1.0$. The width of the domain is 100 units and its height 50 units. The time difference between frames is 8.3 time units or about 1 temporal period of the wave source at the left boundary. One mode each of the first two pairs of Karhunen–Loève modes, obtained from a series of 200 snapshots of a slit simulation that cover an interval of 96 time units or 12 temporal periods of the wave train emitted by the source at the left boundary (and the corresponding “energy content”), are displayed on the right.

we neglect changes in the diffusion coefficient(s) and model the two surface components by allowing for a spatial variation of a kinetic parameter in the model; *i.e.*, we replace the constant b by a space-dependent (sinusoidal or sigmoidal hyperbolic) function $b(x,y)$. When the imposed substrate scale (stripe width) is much smaller than the pattern scale, clearly a transition to some effective behavior is expected. Case studies of coupling of two different excitable media have been investigated in refs 31, 39, and 42, where issues such as transmission of waves across grain boundaries as well as the role of grain boundaries as wave sources were illustrated. In particular, if the boundaries of a lattice of inclusions act as wave sources (“pacemakers”)

for the remaining surface, many symmetric and asymmetric complex spatiotemporal “firing patterns” can arise.^{16,42}

Here we consider composites with stable (as opposed to excitable) individual components; a representative example of such a one-dimensional composite medium (alternating stripes of equal width) is shown in Figure 7. A smooth hyperbolic $b(x)$ dependence approximates a sharp transition between two distinct plateau values of the parameter b : $b_1 = 0.4$ or $b_2 = -0.45$. Both these values of b_1 and b_2 lie outside the range ($-0.24 < b < 0.27$) where oscillatory or excitable behavior (traveling fronts and wave trains) is observed; the arithmetic mean of b_1 and b_2 , however, corresponds to a b value

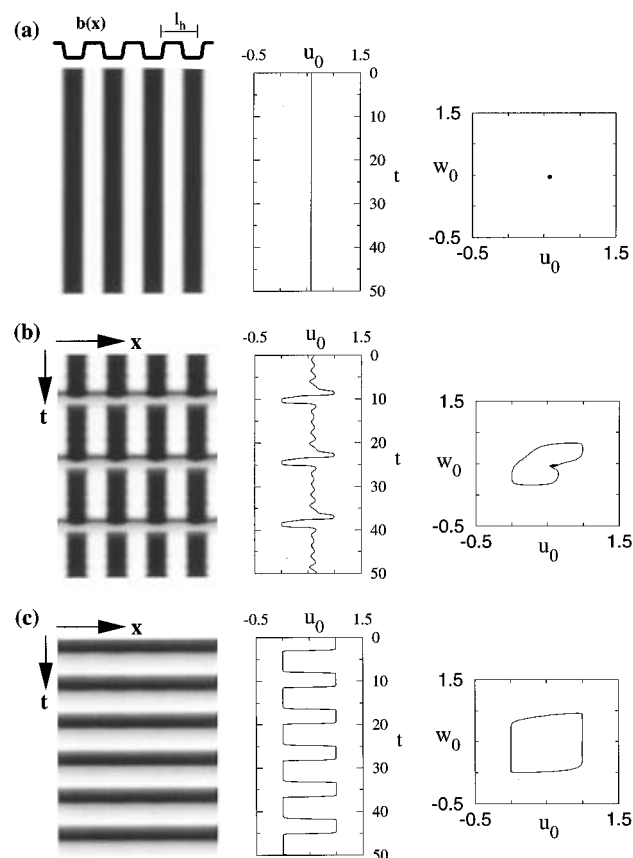


Figure 7. One-dimensional simulations of patterns on a striped composite surface with varying stripe length scale l_h . The parameters are $a = 0.84$, $\epsilon = 0.025$, $b_1 = 0.4$, and $b_2 = -0.45$. Shown are space–time concentration plots, time histories of u_0 , the spatially averaged u , and a phase portrait of the solution in terms of the spatial averages u_0 and w_0 . The range of observed dynamics includes (a) a striped steady state for coarser composites ($l_h = 3.5$), (b) mixed-mode oscillations when the surface alternates between “stripelike” and “effectively uniform” behavior ($l_h = 3.25$), and (c) behavior approaching spatially uniform oscillations (effective medium limit) for a fine-grained composite ($l_h = 1$).

characterized by oscillatory dynamics. Individually, each of these two “media” only supports uniform steady states; a uniform medium with $b = b_1$ exhibits a quiescent steady state (u, w) = (0, 0) whereas a uniform medium with $b = b_2$ supports an ignited state (u, w) = (1, 1).

Keeping the surface composition fixed (at approximately 50% b_1 and 50% b_2 with a smooth hyperbolic transition between the stripes), the dynamics at three different length scales (l_h) are displayed in Figure 7. A steady state pattern of black ($u = 1$) and white ($u = 0$) stripes is shown in Figure 7a ($l_h = 3.5$) which persists for higher l_h . In this limit each individual stripe of the surface evolves toward and remains close to its individual steady state (the steady state of an infinitely extended uniform surface characterized by that value of b); a small diffusion boundary layer exists close to the interface between different stripes. Figure 7c shows the other limit, at a much finer stripe width; here the heterogeneous system exhibits apparently spatially synchronized oscillations in time. At this level of fineness, the composite nature of the surface is no longer visible in the concentration dynamics. Figure 7b displays an intermediate regime, where the oscillatory dynamics of the surface has a mixed character—small, essentially striped oscillations interrupted by periodic, essentially uniform bursts.

The transition scenario between the two limits of steady and oscillatory behavior is very rich, involving so-called mixed-mode oscillations with the concomitant period doubling transi-

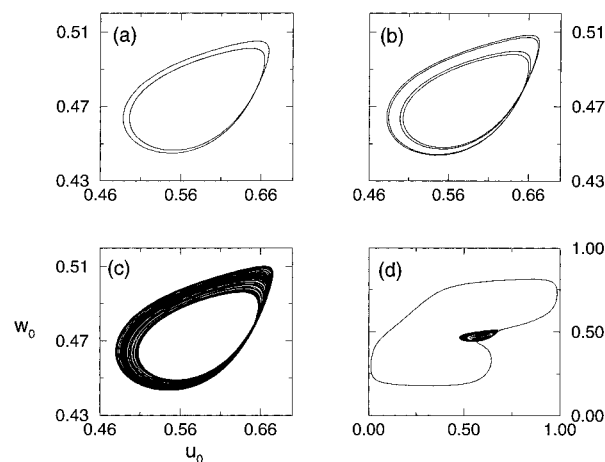


Figure 8. Phase portraits of the solutions on a striped composite surface with varying stripe length scale l_h : (a) period-2 oscillations at $l_h = 3.281$, (b) period-4 oscillations at $l_h = 3.2799$, (c) strange chaotic attractor at $l_h = 3.2795$, (d) crisis induced intermittent bursting at $l_h = 3.2793$.

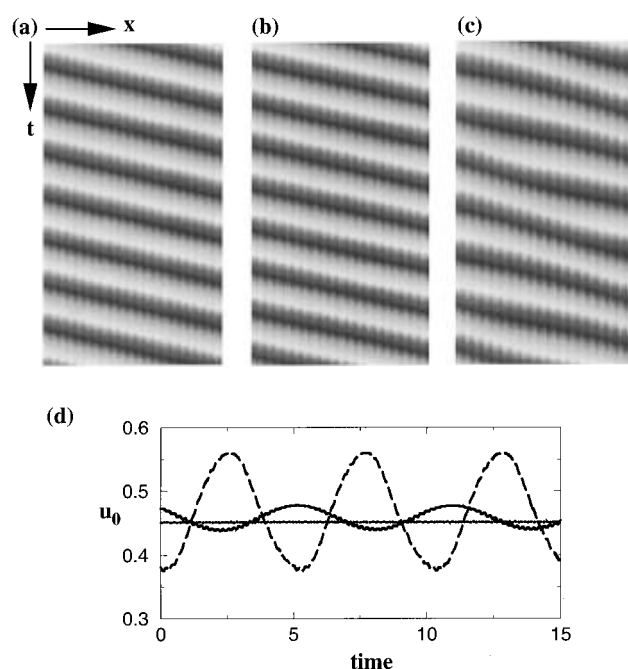


Figure 9. Effect of the “substrate wavelength” of sinusoidal spatial variation of the kinetic parameter b on traveling concentration waves: Model parameters are $a = 0.84$ and $\epsilon = 0.025$; b varies between 0.7 and -0.75 , and the overall domain size (with periodic boundary conditions) is $L = 20$. The sinusoidal substrate wavelengths in dimensionless units are (a) $l_h = 0.95$, (b) $l_h = 1.0$, and (c) $l_h = 1.05$. The lower panel shows time histories of the spatial average u_0 : flat (corresponding to case a), solid line (corresponding to case b), and broken line (corresponding to case c).

tions and Farey sequences. Using the stripe width as a bifurcation parameter (a much more experimentally accessible parameter compared to systematically changing the diffusion coefficient) and starting at the wide stripe limit, the steady pattern first becomes unstable via a supercritical Hopf bifurcation at $l_h \approx 3.34$. The oscillatory limit cycle solution arising at the Hopf bifurcation subsequently undergoes a period-doubling cascade beginning at $l_h \approx 3.28$, and a chaotic attractor with small-amplitude fluctuations is then observed; Figure 8 a,b shows the phase plots of period 2 and period 4 members of this cascade. Figure 8c is a phase plot of the strange chaotic attractor at $l_h = 3.2795$. This chaotic attractor disappears in an internal crisis at about $l_h = 3.2793$ (Figure 8d), and another

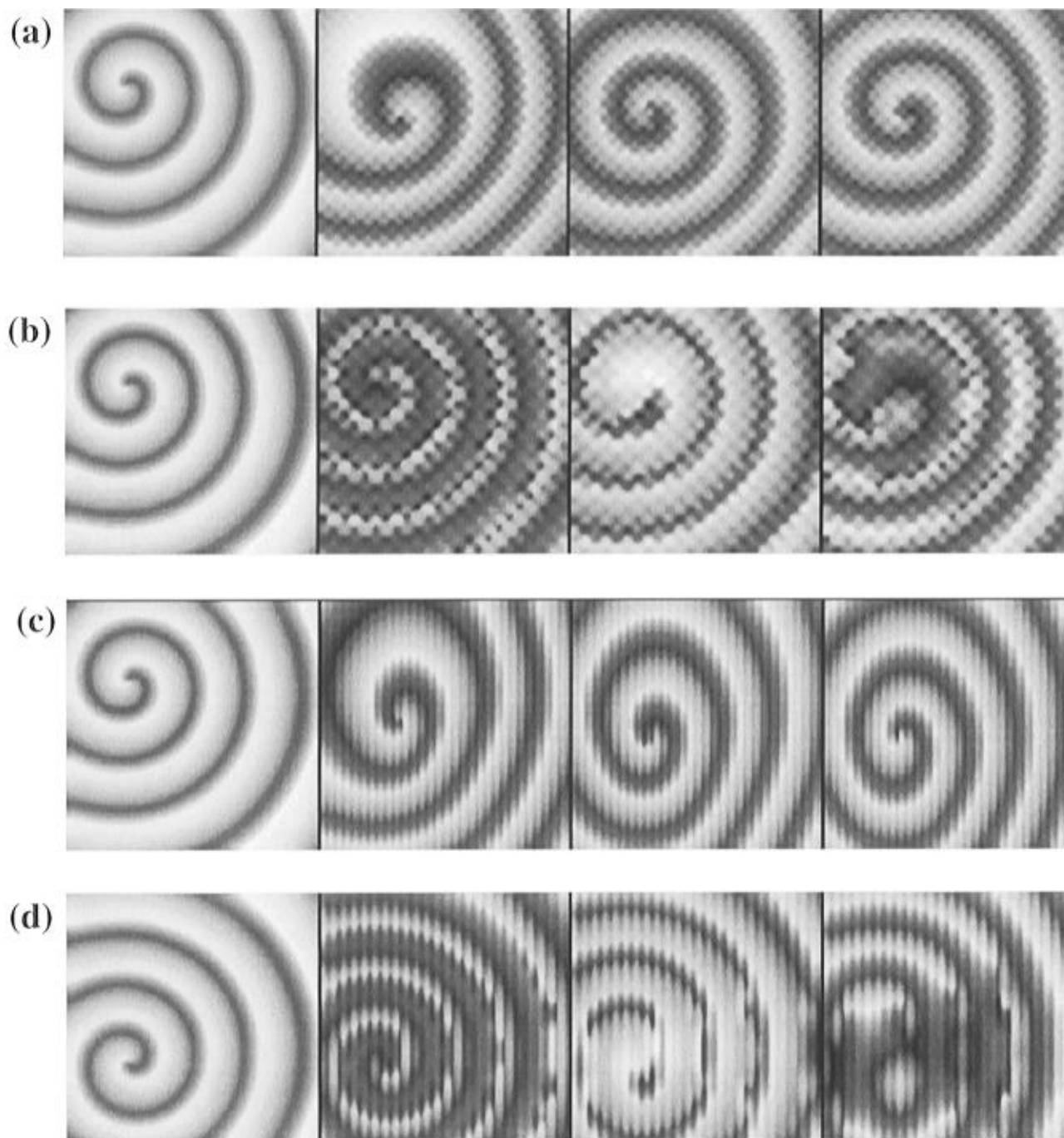


Figure 10. Effect of the “substrate wavelength” of sinusoidal spatial variation of the kinetic parameter b on rotating (spiral) waves. Model parameters are $a = 0.84$ and $\epsilon = 0.025$; b varies between 0.7 and -0.75 , and the square domain has dimensionless side length $L = 40$. The sinusoidal substrate wavelengths (x = horizontal, y = vertical variation) in dimensionless units are (a) $l_h^x = l_h^y = 2.5$, (b) $l_h^x = l_h^y = 3.33$, (c) $l_h^x = 1.33$, and (d) $l_h^x = 1.66$.

chaotic attractor with intermittent excursions to the neighborhoods of both the excited state $(u, w) = (1, 1)$ and the quiescent state $(u, w) = (0, 0)$ is observed. The range $3.279 < l_h < 3.15$ is characterized by mixed-mode oscillations: sequences of small-amplitude oscillations (close to the unstable steady state and thus retaining a “striped” spatial appearance) interrupted by large-amplitude (and spatially more uniform) excursions away from it. Such a scenario has previously been observed by Arneodo *et al.* in reaction–diffusion systems with Dirichlet boundary conditions.⁴³ There the “extinguished” boundaries modulated the excursions of the domain interior to the excited state; here each component of the composite plays the role of “opposite” boundary condition for the other component. The details of the transition scenario as well as the critical length

where the striped steady state goes unstable depend on the “plateau” values b_1 and b_2 as well as on the functional form of the variation. The transition scenario observed in one spatial dimension persists in two dimensions when the two components are spatially distributed in a checkerboard geometry, but the transition values are shifted to larger l_h .

Sinusoidal variations have already been investigated for large rings by Liauw *et al.*³⁹ for the Fitzhugh–Nagumo equation. Steady, visibly “striped” solutions are not so easily realizable for sinusoidal variations; this might be expected, since extensive parts of the domain are at locally excitable or oscillatory conditions. While the effective medium limit is quite similar, for several types of sinusoidal variation in our case we have not observed the mixed-mode bursting instability scenario.

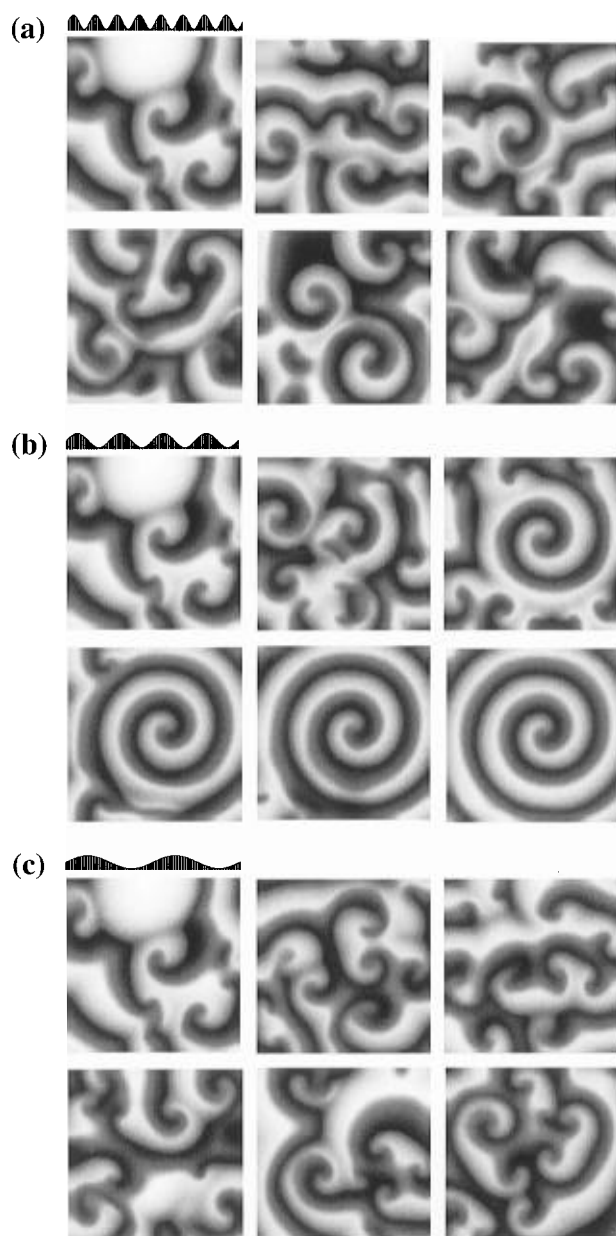


Figure 11. Effect of the “substrate wavelength” of sinusoidal spatial variation of the kinetic parameter b on spatiotemporally chaotic states: The panel sequences show the time evolution of an initial condition chosen from a spatiotemporally chaotic simulation of a uniform ($\epsilon = 0.08$) medium. In the simulations ϵ varies sinusoidally in space between 0.075 and 0.085. The “substrate wavelength” of the sinusoidal variation is (a) $l_h = 5$, (b) $l_h = 10$, and (c) $l_h = 20$ dimensionless space units. The snapshots are 16 spiral periods apart. Stabilization of spiral defects through emergence of effective rotating waves is observed in (b).

As the heterogeneous stripes become thinner, in addition to global, essentially uniform “effectively oscillatory” dynamics, “effective wave trains” are also observed (below $l_h \approx 0.95$). These solutions have a traveling nature but are modulated in time and space (their modulation stemming from the broken translational symmetry of the medium); they become unstable if the length of the individual stripes is increased. Notice that the width of the “effective pulse” here is much larger than the stripe width (e.g., 8.4 space units for $l_h = 0.9$). One of the possible instability scenarios for such wave trains is summarized in Figure 9: here the variation $b(x)$ is sinusoidal, with the same average $b = -0.025$ as above, but larger amplitude (0.725). As the wavelength of this sinusoidal spatial variation is gradually increased, an instability becomes visible in the space–time plots

of the modulated wave trains (Figure 9, top). The instability is also clearly seen as a slow modulation of the global average of the reactant concentrations (Figure 9, bottom). The bifurcation in this case appears to be a supercritical Hopf from a limit cycle (modulated wave train) to a torus; the amplitude of this second modulation is clearly increasing. The period of the “effective” wave train near the instability has a value of 4.1 time units, which is smaller than the period of the “effective” homogeneous oscillation (6.3 time units). The observed instability in Figure 9 should therefore not be related to the instability of wave trains at large periods (comparable to the period of homogeneous oscillations) in oscillatory media.

In two dimensions, one would expect stable spirals in a checkerboard geometry if the substrate length scale is small enough. Figure 10a shows an “effective spiral” on such a sinusoidally spatially modulated checkerboard surface; the substrate variation scale is visually obvious in the figure, which has been obtained starting with a uniform surface ($b = -0.025$) spiral initial condition and then imposing the spatially varying $b(x)$. Increasing the substrate length scale again eventually leads to the disintegration of the effective spiral waves (Figure 10b). We also considered striped geometries (Figure 10c,d), where similar effective spirals can be seen at sufficiently small stripe width; in contrast to the checkerboard case, here the spirals are distinctly anisotropic ($\lambda_x/\lambda_y \sim 5/4$).

We also considered the effect of spatially modulated properties in cases where spirals in a uniform extended domain are unstable (at higher values of the parameter ϵ^{40}). At $\epsilon = 0.08$, our simplified model does not predict stable spirals on a uniform substrate; the dynamics of the surface has a spatiotemporally chaotic character, accentuated by the presence of many “spiral defects”. We now modulate the properties of the medium that gave rise to “chemical turbulence” through spatial variation of ϵ : the uniform medium at $\epsilon = 0.08$ is replaced by unidirectional sinusoidal variations $\epsilon(x) = 0.08 + 0.005 \sin(2\pi x/l_h)$. Such a spatial variation in ϵ amounts to a local variation in the relative reaction rates of u (activator) and w (inhibitor). The ratio of substrate length scale l_h to the (unstable) spiral wavelength (λ) again plays a decisive role in determining pattern dynamics. When the scale variation is small ($l_h < \lambda$), the medium still gives rise to turbulence (effectively comparable to that at $\epsilon \approx 0.08$). Figure 11a shows a series of snapshots from numerical simulations of this case: the spatiotemporally turbulent state persists. When substrate variations occur on a large scale ($l_h > \lambda$), certain spiral centers organize along lower- ϵ parts of the domain (see Figure 11c); these spiral centers are short-lived, and turbulence persists over most of the surface. If the two scales are comparable ($l_h \approx \lambda$), however, the spatiotemporal dynamics can be significantly altered. Starting from a turbulent state with many spiral defects on the surface, a small number of stable effective spirals quickly emerge and annihilate all defects (Figure 11b).

VII. Discussion

Spatiotemporal pattern formation in complicated and composite geometries with active/passive or active/active components is a fascinating subject; in this paper we have presented a brief representative sampling of experimental and computational observations of catalytic pattern formation during CO oxidation on microdesigned Pt metal crystal surfaces. When the substrate length scales (imposed in our case experimentally through microelectronics fabrication techniques) become comparable to spontaneously arising dynamic length scales (due to reaction–diffusion instabilities), pattern dynamics can be modified or even radically altered (e.g., refs 11, 32, 42, 34, 31, 39,

and 44 as well as the examples presented here). The ability to control the geometry and composition of such composites (boundary shape and size, choice of tiling, choice of number and type of components, choice of activity profiles) presents an immensely rich “design parameter” space, and the obvious path is to use these new degrees of freedom not only to explore phenomenology but also to actively influence spatiotemporal dynamics. In the case of catalytic reactions, for example, multifunctional catalysts dispersed at atomic cluster scales are necessary to carry out complex reactions. It is conceivable that microscale composite catalyst surfaces, on which surface diffusion serves as the coupling mechanism, could be designed to optimize features such as overall reactivity and selectivity; this is a direction we are actively pursuing. A new dimension is added to this extensive “medium design” space through spatiotemporal forcing; if we think of variations in the medium as a means of affecting the spontaneously arising patterns, a microdesigned composite surface is only a single, frozen in time, “instruction”. Spatiotemporal variation of the medium properties (whether in open loop or in real-time feedback) provides a much richer set of possibilities for affecting, controlling, and even prescribing system dynamics. Distributed feedback for nonlinear dissipative partial differential equations is not a mature field; these pattern-forming systems, especially through the “bridge” of low-dimensional projection methods, should provide motivation for new research in the systems and control area (see, for example, refs 46–48). In our group we use a laser beam whose focal point and intensity can be modulated to locally heat the Pt surface and thus affect the local reaction rate constants; we also know that a digital projector is used in Prof. Swinney’s group at Austin to “talk to” a photosensitive reaction.

The techniques we have discussed in this paper are not limited to CO oxidation or to low-pressure isothermal catalysis. The study of composite catalysts has already been extended to other surface reactions (e.g., to the NO reduction with CO⁴⁴), and recently developed methods for the observation of catalytic pattern formation at atmospheric pressures⁴⁵ should also combine fruitfully with techniques for constructing microdesigned surfaces.

Acknowledgment. This work was partially supported by the National Science Foundation and by DuPont. The hospitality of the Center of Nonlinear Studies at Los Alamos National Laboratory is gratefully acknowledged, as is the assistance of Michael Lange in catalyst preparation and the contribution of Professor M. D. Graham, Dr. J. Lauterbach, and Dr. K. Asakura at earlier stages of this work.

References and Notes

- (1) Cross, M. C.; Hohenberg, P. C. *Rev. Mod. Phys.* **1993**, *65*, 851.
- (2) Kapral, R.; Showalter, K., Eds. *Chemical Waves and Patterns*; Kluwer: Dordrecht, 1995.
- (3) Mikhailov, A. S. *Foundations of Synergetics I*; Springer-Verlag: Berlin, 1990.
- (4) Hagberg, A.; Meron, E.; Rubinstein, I.; Zaltzman, B. *Phys. Rev. Lett.* **1996**, *76*, 427.
- (5) Couillet, P.; Emilsson, K. *Physica A* **1992**, *188*, 190.
- (6) Battogtokh, D.; Mikhailov, A. S. *Physica D* **1996**, *90*, 84.
- (7) Graham, M.; Kevrekidis, I. G.; Asakura, K.; Lauterbach, J.; Krischer, K.; Rotermund, H. H.; Ertl, G. *Science* **1994**, *264*, 80.
- (8) Graham, M.; Bär, M.; Kevrekidis, I. G.; Asakura, K.; Lauterbach, J.; Rotermund, H.-H.; Ertl, G. *Phys. Rev. E* **1995**, *52*, 76.
- (9) Xin, J. X. *J. Stat. Phys.* **1993**, *73*, 893. Xin, J. X.; Zhu, J. *Physica D* **1995**, *81*, 94. Schütz, P.; Bode, M.; Purwins, H.-G. *Physica D* **1995**, *82*, 382.
- (10) Zhabotinsky, A. M.; Eager, M. D.; Epstein, I. R. *Phys. Rev. Lett.* **1993**, *71*, 1526.
- (11) Voroney, J. P. Masters Thesis, University of Guelph, 1995. Voroney, J. P.; Lawniczak, A.; Kapral, R. *Physica D*, in press.
- (12) Maselko, J.; Showalter, K. *Physica D* **1991**, *49*, 21.
- (13) Lowe, M.; Gollub, J. P. *Phys. Rev. Lett.* **1985**, *51*, 786.
- (14) Hartung, G.; Busse, F. H.; Rehberg, I. *Phys. Rev. Lett.* **1991**, *66*, 2741.
- (15) Schmitz, R.; Zimmermann, W. *Phys. Rev. E* **1996**, *53*, R1321.
- (16) Hess, O.; Schöll, E. *Physica D* **1994**, *70*, 165. Merbach, D.; Hess, O.; Herzel, H.; Schöll, E. *Phys. Rev. E* **1995**, *52*, 1571.
- (17) Ertl, G. *Science* **1991**, *254*, 1750.
- (18) Imbihl, R.; Ertl, G. *Chem. Rev.* **1995**, *95*, 697.
- (19) Eiswirth, M.; Ertl, G. In *Chemical Waves and Patterns*; Kapral, R.; Showalter, K., Eds.; Kluwer: Dordrecht, 1995.
- (20) Jakubith, S.; Rotermund, H. H.; Engle, W.; von Oertzen, Ertl, G. *Phys. Rev. Lett.* **1990**, *65*, 3013.
- (21) Nettesheim, S.; von Oertzen, A.; Rotermund, H.-H.; Ertl, G. *J. Chem. Phys.* **1993**, *98*, 9977.
- (22) Engel, W.; Kordes, M. E.; Rotermund, H. H.; Kubala, S.; von Oertzen, A. *Ultramicroscopy* **1991**, *36*, 148.
- (23) Engel, T.; Ertl, G. *Adv. Catal.* **1979**, *28*, 1.
- (24) Krischer, K.; Eiswirth, M.; Ertl, G. *J. Chem. Phys.* **1992**, *97*, 303.
- (25) Bär, M.; Gottschalk, N.; Eiswirth, M.; Ertl, G. *J. Chem. Phys.* **1994**, *100*, 1202.
- (26) Malchow, H.; Schimansky-Geier, L. *Noise and Diffusion in Bistable Nonequilibrium Systems*; Teubner: Berlin, 1985.
- (27) Leis, J. R.; Kramer, M. A. *ACM Trans. Math. Software* **1988**, *14*, 61.
- (28) Bär, M.; Nettesheim, S.; Rotermund, H. H.; Eiswirth, M.; Ertl, G. *Phys. Rev. Lett.* **1995**, *74*, 1246.
- (29) Zaikin, A. N.; Zhabotinsky, A. M. *Nature* **1970**, *225*, 535.
- (30) Krinsky, V. I.; Agladze, K. I. *Physica D* **1983**, *8*, 50.
- (31) Bär, M.; Kevrekidis, Y.; Rotermund, H. H.; Ertl, G. *Phys. Rev. E* **1995**, *52*, R 5739.
- (32) Haas, G.; Bär, M.; Kevrekidis, I. G.; Rasmussen, P. B.; Rotermund, H. H.; Ertl, G. *Phys. Rev. Lett.* **1995**, *75*, 3560.
- (33) Tyson, J. J.; Keener, J. P. *Physica D* **1988**, *32*, 327.
- (34) Agladze, K.; Keener, J. P.; Müller, S. C.; Panflov, A. *Science* **1994**, *264*, 1746.
- (35) Fukunaga, K. *Introduction to Statistical Pattern Recognition*; Academic Press: New York, 1990.
- (36) Asakura, K.; Lauterbach, J.; Rotermund, H. H.; Ertl, G. *Phys. Rev. B* **1994**, *50*, 8043.
- (37) Asakura, K.; Lauterbach, J.; Rotermund, H. H.; Ertl, G. *J. Chem. Phys.* **1995**, *102*, 8175.
- (38) Steinbock, O.; Kettunen, P.; Showalter, K. *Science* **1995**, *269*, 1857.
- (39) Liauw, M.; Ning, J.; Luss, D. *J. Chem. Phys.* **1996**, *104*, 5657.
- (40) Bär, M.; Eiswirth, M. *Phys. Rev. E* **1993**, *48*, 1635.
- (41) Skinner, G. S.; Swinney, H. L. *Physica D* **1991**, *48*, 1. Engel, H.; Braune, M. *Phys. Scr.* **1993**, *T49*, 685.
- (42) Bangia, A. K.; Bär, M.; Kevrekidis, I. G.; Graham, M. D.; Rotermund, H. H.; Ertl, G. *Chem. Eng. Sci.* **1996**, *51*, 1757.
- (43) Elezgaray, J.; Arneodo, A. *Phys. Rev. Lett.* **1992**, *68*, 714.
- (44) Hartmann, N.; Bär, M.; Kevrekidis, I. G.; Krischer, K.; Imbihl, R. *Phys. Rev. Lett.* **1996**, *76*, 1384.
- (45) Rotermund, H. H.; Haas, G.; Franz, R. U.; Tromp, R. M.; Ertl, G. *Science* **1995**, *270*, 608.
- (46) Gay, D. H.; Ray, W. H. *Chem. Eng. Sci.* **1995**, *50*, 1519.
- (47) Chen, C. C.; Chang, H.-C. *AIChE J.* **1992**, *38*, 1461.
- (48) Christophides, P. D.; Daoutidis, P. *Comput. Chem. Eng.* **1996**, *20*, S1071.

JP961689Q